INTERNATIONAL JOURNAL FOR NUMERICAL METHODS IN ENGINEERING
Int. J. Numer. Meth. Engng 2005; **62**:700–726
Published online 3 December 2004 in Wiley InterScience (www.interscience.wiley.com). DOI: 10.1002/nme.1216

Equivalent localization element for crack band approach to mesh-sensitivity in microplane model

Jan Červenka[1], Zdeněk P. Bažant[2,*,†,‡] and Martin Wierer[3,§]

[1]*Červenka Consulting, Predvoje 22, 162 00, Prague, Czech Republic*
[2]*Departments of Civil Engineering and Materials Science, 2135 Sheridan Road, CEE, Northwestern University, Evanston, IL 60208, U.S.A.*
[3]*Institute of Structural Mechanics, Czech Technical University, Prague, Czech Republic*

SUMMARY

The paper presents in detail a novel method for finite element analysis of materials undergoing strain-softening damage based on the crack band concept. The method allows applying complex material models, such as the microplane model for concrete or rock, in finite element calculations with variable finite element sizes not smaller than the localized crack band width (corresponding to the material characteristic length). The method uses special localization elements in which a zone of characteristic size, undergoing strain softening, is coupled with layers (called 'springs') which undergo elastic unloading and are normal to the principal stress directions. Because of the coupling of strain-softening zone with elastic layers, the computations of the microplane model need to be iterated in each finite element in each load step, which increases the computer time. Insensitivity of the proposed method to mesh size is demonstrated by numerical examples. Simulation of various experimental results is shown to give good agreement. Copyright © 2004 John Wiley & Sons, Ltd.

KEY WORDS: fracture; damage; concrete; microplane model; finite elements; localization

1. INTRODUCTION

Quasibrittle materials, such as concrete, mortar, rock or masonry, exhibit strain softening in the post-peak response, both in tension and in compression. In finite element modelling, a consequence of strain softening is spurious sensitivity of the results to the mesh size. If

*Correspondence to: Z. P. Bažant, McCormick School Professor and W. P. Murphy, Professor of Civil Engineering and Materials Science, 2135 Sheridan Road, CEE, North-western University, Evanston, IL 60208, U.S.A.
†E-mail: z-bazant@northwestern.edu
‡Formerly Visiting Scholar, Northwestern University.
§Formerly Visiting Predoctoral Fellow, Northwestern University, and Research Associate, Červenka Consulting, Předvoje 22, 162 00, Prague, Czech Republic.

Contract/grant sponsor: U.S. National Science Foundation (NSF); contract/grant numbers: CMS-9732791, CMS-030145
Contract/grant sponsor: Czech Grant Agency; contract/grant number: 103/99/0755

Received 1 November 2001
Revised 16 June 2004
Accepted 11 August 2004

a material model with strain-softening is defined solely in terms of the stress–strain relations, the energy that is dissipated during brittle failure in the critical regions of localized strain-softening damage will decrease with mesh refinement. In the limit of a vanishing finite element size, this can result in zero energy dissipation during failure, which is physically impossible. The spurious mesh sensitivity is caused by ill-posedness of the boundary value problem. In non-linear numerical solutions by the finite element method, which usually involve some sort of an iterative algorithm, the ill-posedness gets manifested by loss of convergence.

One remedy for the spurious mesh sensitivity caused by strain softening due to smeared tensile cracking is the crack band model of Bažant [1, 2] and Bažant and Oh [3] (see also Bažant and Planas [4]). The basic idea of this model for strain-softening in tension (and also of the model of Pietruszczak and Mroz [5] for strain-softening in shear) is to modify the material parameters controlling the smeared cracking such that the energies dissipated by large and small elements per unit area of the crack band would be identical. A more general remedy, which also avoids mesh orientation bias, is the non-local model (Bažant [6], Pijaudier-Cabot and Bažant [7], Bažant and Jirásek [8]), which is appropriate when small enough elements subdividing the crack band (and resolving the strain distribution within the band) need to be used.

Of these two remedies, the crack band model dominates in concrete design practice by far because it is easier to program and computationally less demanding. In commercial finite element codes, however, the crack band model is currently employed only in combination with relatively simple and inaccurate material models. The recent more advanced material models considered in research are normally implemented within some type of non-local framework. These models can usually simulate rather complex loading scenarios, but their application to practical engineering problems is difficult, due to the requirement that the finite element size in the failure zone should be significantly less than the characteristic length of the material, which is, in the present context, understood as the minimum possible spacing of parallel cohesive cracks and is equal to approximately 1.5 times the maximum aggregate size (this length must be distinguished from Irwin's characteristic length, which characterizes the length of the fracture process zone [4, 8]. For real-life structures, this requirement leads to a very large number of elements, although this can be mitigated by some elaborate adaptive scheme.

The crack band model is not easy to apply to complex material models in its current form, because for such models it is not easy to identify which material parameters should be adjusted according to the element size to ensure correct energy dissipation in the softening regime. A typical material model of this kind is the microplane model, the initial version of which was developed by Bažant [9] who adapted a general idea of Taylor [10]. This model contains parameters that were calibrated for finite element sizes close to the material characteristic length and cannot be easily adjusted for very different element sizes.

This paper, the basic idea of which was briefly outlined at a recent conference (Bažant *et al*. [11]), presents a novel method that makes it easy to apply the microplane model when the finite elements in the damage zone are much larger then the material characteristic length. Applicable though the present method is to other material models and other materials, this paper deals only with applications to the microplane model and to concrete. Version M4 of the microplane model for concrete [12] is used in all the numerical computations throughout this paper.

2. CRACK BAND MODEL

In the crack band model [3], the material parameters are adjusted such that the same amount of energy is dissipated during failures of a large and small finite element. The adjustment is based on the assumption that a single localization band (i.e. a cohesive crack) develops inside the element. Based on this assumption, the crack opening displacement w can be calculated from the fracturing strain ε^{f} using the following simple formula:

$$w = L\varepsilon^{\mathrm{f}} \tag{1}$$

where L is the crack band size (width), which can be determined on the basis of the finite element size projected onto the direction of the maximum principal strain for the case of tensile cracking and low-order finite elements.

3. MICROPLANE MODEL

The basic idea of the microplane model is to abandon constitutive modeling in terms of tensors and their invariants and formulate the stress–strain relation in terms of stress and strain vectors acting on planes of various orientations in the material, now generally called the microplanes (Figure 1 top left). This idea arose in Taylor's [10] pioneering study of hardening plasticity of polycrystalline metals. Proposing the first version of the microplane model, Bažant [9], in order to model strain softening in quasibrittle materials with heterogenous microstructure (Figure 1 top middle), extended and modified Taylor's model in several ways (in detail see Bažant *et al*. [12]). The main one was the use of a kinematic constraint between the strain tensor and the microplane strain vectors (instead of a static constraint used in Taylor models for plasticity of polycrystalls). Since 1984, there have been numerous improvements and variations of the microplane approach. A detailed overview of the history of the microplane model is included in Bažant *et al*. [12] and Caner and Bažant [13]. In what follows, we briefly review the derivation of the microplane model that is used in this work.

In the microplane model, the constitutive equations are formulated on a plane, called microplane, having an arbitrary orientation characterized by its unit normal n_i. The kinematic constraint means that the normal strain ε_N and shear strains ε_M, ε_L on the microplane are calculated as the projections of the macroscopic strain tensor ε_{ij}:

$$\varepsilon_N = n_i n_j \varepsilon_{ij}, \quad \varepsilon_M = \tfrac{1}{2}(m_i n_j + m_j n_i)\varepsilon_{ij}, \quad \varepsilon_L = \tfrac{1}{2}(l_i n_j + l_j n_i)\varepsilon_{ij} \tag{2}$$

where m_i and l_i are chosen orthogonal vectors lying in the microplane and defining the shear strain components (Figure 1 top left). The constitutive relations for the microplane strains and stresses can be generally stated as

$$\begin{aligned} \sigma_N(t) &= F^t_{\tau=0}[\varepsilon_N(\tau), \varepsilon_L(\tau), \varepsilon_M(\tau)] \\ \sigma_M(t) &= G^t_{\tau=0}[\varepsilon_N(\tau), \varepsilon_L(\tau), \varepsilon_M(\tau)] \\ \sigma_L(t) &= G^t_{\tau=0}[\varepsilon_N(\tau), \varepsilon_L(\tau), \varepsilon_M(\tau)] \end{aligned} \tag{3}$$

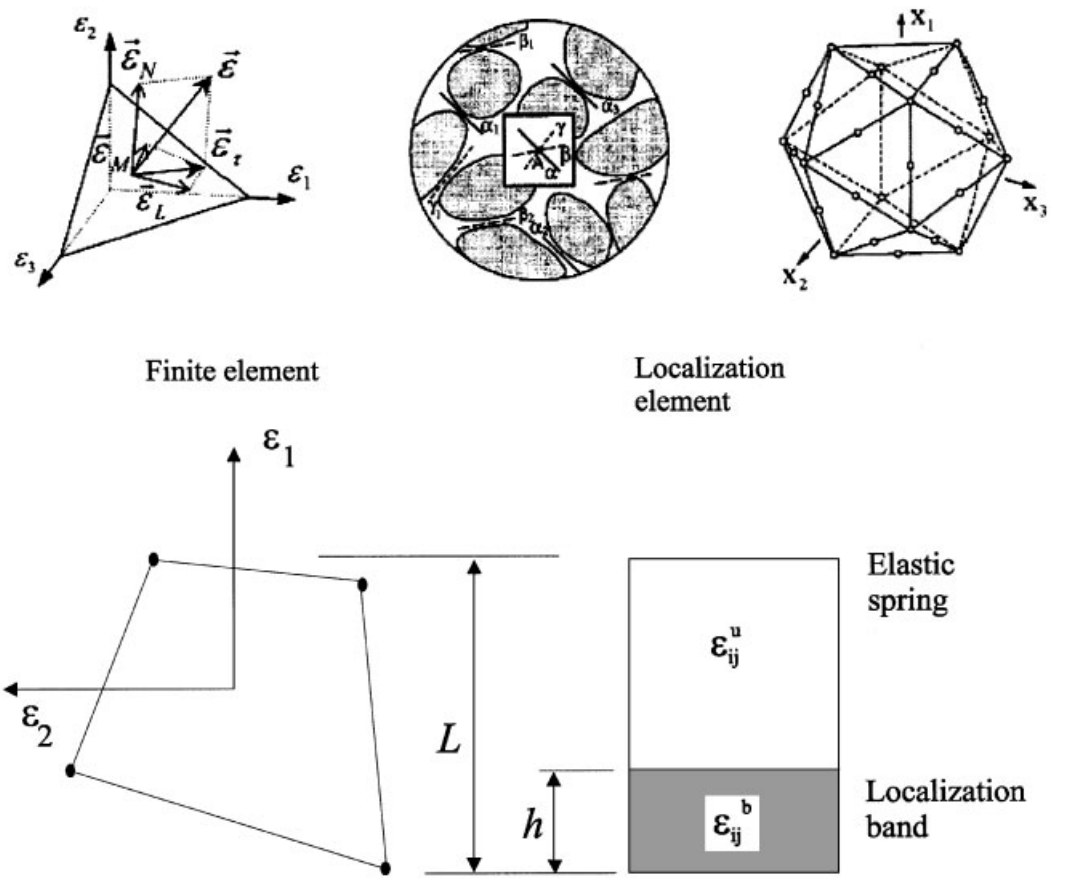

Figure 1. Top: left: Microplane with its stress or strain vector; middle: heterogeneous microstructures smeared by microplane model; right: efficient 21-point Gaussian numerical integration formula for spherical surface derived by Bažant and Oh [3]; bottom: equivalent localization element.

where F and G are functionals of the history of the microplane strains in time t. For a detailed derivation of these functionals a reader is referred to Bažant *et al.* [12] and Caner and Bažant [13]. The macroscopic stress tensor is obtained by the principle of virtual work that is applied to a unit hemisphere Ω. After the integration, the following expression for the macroscopic stress tensor is recovered [9]:

$$\sigma_{ij}=\frac{3}{2\pi}\int_{\Omega} s_{ij}\,\mathrm{d}\Omega \approx 6\sum_{\mu=1}^{N_m} w_\mu s_{ij}^{(\mu)}, \quad \text{where } s_{ij}=\sigma_N n_i n_j+\frac{\sigma_M}{2}(m_i n_j+m_j n_i)+\frac{\sigma_L}{2}(l_i n_j+l_j n_i) \tag{4}$$

where the integral is approximated by an optimal Gaussian integration formula for a spherical surface; numbers μ label the points of the integration formula and w_μ are the corresponding

optimal weights. An example of an efficient 21-point formula (derived by Bažant and Oh, 1985) is shown in Figure 1 (top right) where the circles represent the integration points corresponding to the directions of microplane normals.

Version M4 of the microplane model has been implemented into a commercial finite element code, called ATENA. This code is used in all the examples throughout this paper.

4. ONE-DIMENSIONAL EQUIVALENT ELEMENT

The objective of the equivalent localization element is to achieve equivalence with the crack band model. This basic idea is that the material properties and parameters of the softening material model are not modified to account for the differences in the finite element size, but rather the softening crack band is coupled as a layer with an elastically behaving zone, in order to obtain equivalence. For brevity, this zone will henceforth be called the 'spring'. For large finite elements, the effective length of this added elastic spring, representing the width of the added elastic zone having the elastic properties of the material, will be much larger than the size (or thickness) of the localization zone (crack band). Thus, after the crack initiation, the energy stored in the elastic spring can be readily transferred to the localization zone and dissipated in the softening (i.e. fracturing) process.

Inside each finite element, at each integration point, an equivalent localization element is assumed. The localization element is a serial arrangement of the localization zone, which is loading, and an elastic zone (spring), which is unloading. The total length of the element is equivalent to the crack band size L (width), and can be determined using the same methods as described in Section 2 (see Figure 1). The width of the localization zone is given either by the characteristic length of the material or by the size of the test specimen for which the adopted material model has been calibrated. The direction of the localization element, given by the normal to the localization and elastic zones, should be perpendicular to the plane of failure propagation. An appropriate definition of this direction is important and not trivial, and it will be discussed later in this paper. For the time being, let us assume that the direction of failure propagation is known. The direction of crack propagation is denoted by subscript 2 and the direction of the localization element by subscript 1 in the subsequent derivations.

The strain vector can be separated into two parts: the vector of strains in the elastic spring, which will unload during localization and will be denoted by superscript u, and the vector of strains in the localization band, which will be denoted by superscript b.

The displacement compatibility condition for the whole length of the equivalent localization element gives the following relationship between the finite element strain vector $\boldsymbol{\varepsilon}$, the elastic spring strain vector $\boldsymbol{\varepsilon}^u$, and the strain vector in the localization band $\boldsymbol{\varepsilon}^b$:

$$L\boldsymbol{\varepsilon} = h\boldsymbol{\varepsilon}^b + (L - h)\boldsymbol{\varepsilon}^u \tag{5}$$

where h is the width of the localization band. The components of the strain and stress vectors are assumed to be transformed into a frame defined by directions 1 and 2, and are arranged in the following manner:

$$\boldsymbol{\varepsilon} = \{\xi, \boldsymbol{\eta}\}^{\mathrm{T}} \quad \text{and} \quad \boldsymbol{\sigma} = \{\mathbf{s}, \mathbf{t}\}^{\mathrm{T}} \tag{6}$$

where

$$\boldsymbol{\xi} = \{\varepsilon_{11}, 2\varepsilon_{12}, 2\varepsilon_{13}\}^{\mathrm{T}}, \quad \boldsymbol{\eta} = \{\varepsilon_{22}, \varepsilon_{33}, 2\varepsilon_{23}\}^{\mathrm{T}} \tag{7}$$

$$\mathbf{s} = \{\sigma_{11}, \sigma_{12}, \sigma_{13}\}^{\mathrm{T}}, \quad \mathbf{t} = \{\sigma_{22}, \sigma_{33}, \sigma_{23}\}^{\mathrm{T}} \tag{8}$$

Using the foregoing stress and strain vector components, one can define the corresponding submatrices of the constitutive matrix by analogy;

$$\boldsymbol{\sigma} = \begin{Bmatrix} \mathbf{s} \\ \mathbf{t} \end{Bmatrix} = \mathbf{D} \begin{Bmatrix} \boldsymbol{\xi} \\ \boldsymbol{\eta} \end{Bmatrix} = \begin{bmatrix} \mathbf{D}^{ss} & \mathbf{D}^{st} \\ \mathbf{D}^{ts} & \mathbf{D}^{tt} \end{bmatrix} \begin{Bmatrix} \boldsymbol{\xi} \\ \boldsymbol{\eta} \end{Bmatrix} \tag{9}$$

where $\mathbf{D}$ means generally the secant stiffness matrix. The localization element is considered only in direction 1, which is perpendicular to the plane of failure propagation. This implies, for the components of the strain vectors, the conditions:

$$L\boldsymbol{\xi} = h\boldsymbol{\xi}^b + (L-h)\boldsymbol{\xi}^u \tag{10}$$

$$\boldsymbol{\eta} = \boldsymbol{\eta}^b = \boldsymbol{\eta}^u \tag{11}$$

and for the components of the stress vectors the conditions:

$$\mathbf{s} = \mathbf{s}^b = \mathbf{s}^u \tag{12}$$

$$\mathbf{t} = \frac{h}{L}\,\mathbf{t}^b + \frac{L-h}{L}\,\mathbf{t}^u \tag{13}$$

The equilibrium condition (12) must be satisfied by the stresses in the elastic and localization zones. The stresses in the elastic zone are easily calculated using the elastic constitutive matrix.

$$\mathbf{s}^u = \mathbf{s}^{u^0} + [\mathbf{D}^{ss} \;\; \mathbf{D}^{st}] \begin{Bmatrix} \Delta\boldsymbol{\xi}^u \\ \Delta\boldsymbol{\eta} \end{Bmatrix} \tag{14}$$

while the localization zone stresses are determined from the microplane model:

$$\mathbf{s}^b = F^s(\boldsymbol{\varepsilon}^{b^0}, \Delta\boldsymbol{\varepsilon}^b) \tag{15}$$

Equations (10)–(15) form a system of non-linear equations, which can be solved, for instance, by iterations according to the Newton–Raphson method. The objective of the Newton–Raphson method is to minimize the residuals given by Equation (12);

$$\mathbf{r} = \mathbf{s}^b - \mathbf{s}^u \tag{16}$$

The residuals can be rewritten in terms of a truncated Taylor series:

$$\mathbf{r}^{(i+1)} = \mathbf{r}^{(i)} + \frac{\partial \mathbf{r}^{(i)}}{\partial \boldsymbol{\xi}^u}\,\mathbf{d}\boldsymbol{\xi}^u \tag{17}$$

After many iterations, the residuals will, during the iterative process, tend to zero. Therefore it is possible to write the following iterative equation:

$$r^{(i)} + \frac{\partial \mathbf{r}^{(i)}}{\partial \xi^u}\, \mathbf{d}\xi^{u^{(i+1)}} = 0 \tag{18}$$

where $\mathrm{d}\xi^{u^{(i+1)}}$ is an iterative correction of the strain tensor component in the spring. This expression can be solved in each iteration for the new correction of $\mathrm{d}\xi^{u^{(i+1)}}$. After substituting (14) and (15) into (18), the following expression is obtained:

$$\mathbf{r}^{(i)} + \frac{\partial}{\partial \xi^u}\left[F^s(\boldsymbol{\varepsilon}^{b^0}, \Delta\boldsymbol{\varepsilon}^b) - \mathbf{s}^u\right] \mathbf{d}\xi^{u^{(i+1)}} = 0 \tag{19}$$

The derivative of $\mathbf{s}^u$ with respect to ξ^u is equal to $\mathbf{D}^{ss}$. Therefore, the expression can be re-written in the following manner:

$$\mathbf{r}^{(i)} + \left[\frac{\partial}{\partial \xi^u} F^s(\boldsymbol{\varepsilon}^{b^0}, \Delta\boldsymbol{\varepsilon}^b) - \mathbf{D}^{ss}\right] \mathbf{d}\xi^{u^{(i+1)}} = 0 \tag{20}$$

Then the chain rule of differentiation can be applied,

$$\mathbf{r}^{(i)} + \left[\frac{\partial}{\partial \xi^b}\frac{\partial \xi^b}{\partial \xi^u} F^s(\boldsymbol{\varepsilon}^{b^0}, \Delta\boldsymbol{\varepsilon}^b) - \mathbf{D}^{ss}\right] \mathbf{d}\xi^{u^{(i+1)}} = 0 \tag{21}$$

and the following expression that is derived on the basis of Equation (10) can be substituted into formula (21):

$$\frac{\partial \xi^b}{\partial \xi^u} = \frac{h - L}{h} \tag{22}$$

In addition, it is possible to assume that the derivative of $F^s(\boldsymbol{\varepsilon}^b, \Delta\boldsymbol{\varepsilon}^b)$ is equal to

$$\frac{\partial}{\partial \xi^b}\left[F^s(\boldsymbol{\varepsilon}^{b^0}, \Delta\boldsymbol{\varepsilon}^b)\right] = \mathbf{D}^{ss}\mathbf{I} \tag{23}$$

This assumption corresponds to the modified Newton–Raphson scheme, in which the initial elastic stiffness is used throughout the iterative process. The substitutions of (22) and (23) simplify Equation (21) to the following relationship:

$$\mathbf{r}^{(i)} + \left[\frac{h - L}{h}\mathbf{D}^{ss} - \mathbf{D}^{ss}\right] \mathbf{d}\xi^{u^{(i+1)}} = 0 \tag{24}$$

$$\mathbf{r}^{(i)} - \frac{L}{h}\mathbf{D}^{ss}\mathbf{d}\xi^{u^{(i+1)}} = 0 \tag{25}$$

The iterative algorithm will then consist of the following steps:

Step 1:

$$\mathbf{d}\xi^{u^{(i)}} = \frac{h}{L}(\mathbf{D}^{ss})^{(-1)}\mathbf{r}^{(i-1)}$$

Step 2:

$$\Delta\boldsymbol{\xi}^{u^{(i)}} = \Delta\boldsymbol{\xi}^{u^{(i-1)}} + \mathbf{d}\boldsymbol{\xi}^{u^{(i)}}$$

Step 3:

$$\Delta\boldsymbol{\xi}^{b^{(i)}} = \frac{1}{h}\left[L\Delta\boldsymbol{\xi} - (L-h)\Delta\boldsymbol{\xi}^{u^{(i)}}\right]$$

Step 4:

$$\mathbf{r}^{(i)} = F^s(\boldsymbol{\varepsilon}^{b^0}, \Delta\boldsymbol{\varepsilon}^{b^{(i)}}) - \mathbf{s}^{u^{(i)}} \tag{26}$$

The iterations are terminated when the given iteration criteria are satisfied. For the foregoing algorithm the following criteria are suitable:

$$\frac{\|\mathbf{d}\boldsymbol{\xi}^{u^{(i)}}\|}{\|\Delta\boldsymbol{\xi}\|} < e, \quad \frac{\|\mathbf{r}^{(i)}\|}{\|\Delta\mathbf{s}\|} < e, \quad \frac{|\mathbf{r}^{(i)^{\mathrm{T}}}\,\mathbf{d}\boldsymbol{\xi}^{u^{(i)}}|}{\|\Delta\mathbf{s}\Delta\boldsymbol{\xi}\|} < e \tag{27}$$

Once the iterative algorithm (26) has satisfied the prescribed tolerance e, the separation of the total strain tensor into the elastic spring strains and the localization band strain is known. The global stress tensor is then calculated using formulae (12) and (13).

After examination of formulae (12) and (13), note that the stress components on the planes oriented perpendicularly to the localization element are calculated by weighted averaging of the appropriate stress components in the elastic spring and in the localization band (crack band). This would significantly decrease any non-linear response in these orientations from the macroscopic stress tensor, since the elastic spring will 'support' the localization band. Consequently, the one-dimensional equivalent localization element is suitable only for problems, in which the localization causes an increase of only one of the principal strain components while the others remain small and within the elastic regime. In applications to concrete structures, this limits the applicability of the present approach to tensile dominated failure modes such as pure tension or bending.

To alleviate these constraints, the proposed method is extended to a full three-dimensional setting.

5. THREE-DIMENSIONAL EQUIVALENT LOCALIZATION ELEMENT

The method proposed in the preceding section would be applicable only for cases in which the failure causes an increase of only one principal strain component, such as the axial strain due to pure tension or bending. If another strain component increases above its elastic limit, part of the stress is carried by the elastic spring, since for these strain components the arrangement is not serial but parallel. This constraint can be removed by extending the proposed technique into three dimensions (3D), with the equivalent localization elements being applied in three orientations. Ideally, the chosen directions should be perpendicular to the planes of failure propagation. In this work, they are assumed to be aligned with the principal axes of the total macroscopic strain tensor, which in most cases should approximately correspond to the aforementioned requirement.

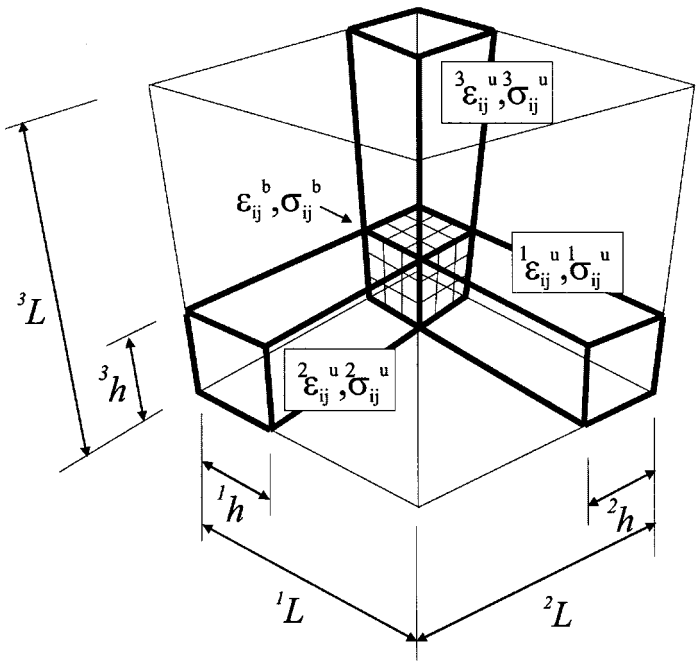

Figure 2. Arrangement of the three-dimensional equivalent localization element.

The three-dimensional equivalent element is constructed in analogy to the one-dimensional case, but this time three serial arrangements of the elastic zone (spring) and localization band are defined. The spring-band systems are perpendicular to each other, and they are arranged parallel to the principal strain directions (Figure 2). The simplified two-dimensional version is shown in Figure 3. In this arrangement of spring-band systems it is possible to identify the following unknown stresses and strains:

$$\sigma_{ij}^b, {}^1\sigma_{ij}^u, {}^2\sigma_{ij}^u, {}^3\sigma_{ij}^u \quad \text{and} \quad \varepsilon_{ij}^b, {}^1\varepsilon_{ij}^u, {}^2\varepsilon_{ij}^u, {}^3\varepsilon_{ij}^u$$

where superscript b denotes the quantities in the localization band and the symbol ${}^m x^u$ with left and right superscripts u and m defines the quantities in the elastic spring in the direction m.

Altogether there are 48 unknown variables. In the subsequent derivations, it is assumed that these stresses and strains are defined in the principal frame of the total macroscopic strain tensor. The set of equations available for determining these variables starts with the constitutive formulae for the band and the elastic springs:

$$\sigma_{ij}^b = F(\varepsilon_{ij}^b) \tag{28}$$

$${}^m\sigma_{ij}^u = D_{ijlk}\, {}^m\varepsilon_{kl}^u \quad \text{for } m = 1, \ldots 3 \tag{29}$$

The first formula (28) represents the evaluation of the non-linear material model, which in our case is the microplane model for concrete. The second Equation (29) is a set of three elastic

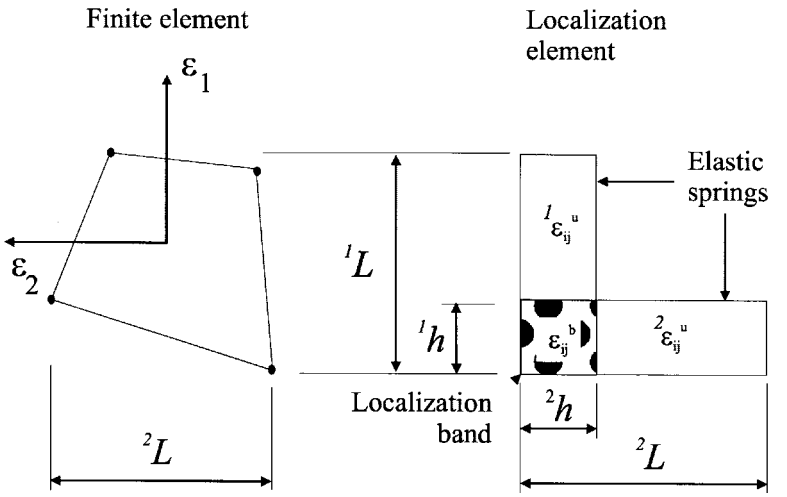

Figure 3. Simplified two-dimensional view of the spring—crack band arrangement.

constitutive formulations for the three linear zones (springs) that are involved in the arrangement in Figure 2. This provides the first 24 equations, which can be used for the calculation of unknown strains and stresses.

The second set of equations is provided by the kinematic constrains on the strain tensors;

$$
\begin{aligned}
\varepsilon_{11} &= \frac{1}{{}^1L}\left[\varepsilon_{11}^{b}\,{}^1h + {}^1\varepsilon_{11}^{u}\left({}^1L - {}^1h\right)\right]\\
\varepsilon_{22} &= \frac{1}{{}^2L}\left[\varepsilon_{22}^{b}\,{}^2h + {}^2\varepsilon_{22}^{u}\left({}^2L - {}^2h\right)\right]\\
\varepsilon_{33} &= \frac{1}{{}^3L}\left[\varepsilon_{33}^{b}\,{}^3h + {}^3\varepsilon_{33}^{u}\left({}^3L - {}^3h\right)\right]\\
\varepsilon_{12} &= \frac{1}{2}\left\{\frac{1}{{}^1L}\left[\varepsilon_{12}^{b}\,{}^1h + {}^1\varepsilon_{12}^{u}\left({}^1L - {}^1h\right)\right] + \frac{1}{{}^2L}\left[\varepsilon_{12}^{b}\,{}^2h + {}^2\varepsilon_{12}^{u}\left({}^2L - {}^2h\right)\right]\right\}\\
\varepsilon_{23} &= \frac{1}{2}\left\{\frac{1}{{}^2L}\left[\varepsilon_{23}^{b}\,{}^2h + {}^2\varepsilon_{23}^{u}\left({}^2L - {}^2h\right)\right] + \frac{1}{{}^3L}\left[\varepsilon_{23}^{b}\,{}^3h + {}^3\varepsilon_{23}^{u}\left({}^3L - {}^3h\right)\right]\right\}\\
\varepsilon_{13} &= \frac{1}{2}\left\{\frac{1}{{}^1L}\left[\varepsilon_{13}^{b}\,{}^1h + {}^1\varepsilon_{13}^{u}\left({}^1L - {}^1h\right)\right] + \frac{1}{{}^3L}\left[\varepsilon_{13}^{b}\,{}^3h + {}^3\varepsilon_{13}^{u}\left({}^3L - {}^3h\right)\right]\right\}
\end{aligned}
\tag{30}
$$

These six additional equations can be written symbolically as

$$
\varepsilon_{ij} = \frac{1}{2}\left\{\frac{1}{{}^iL}\left[\varepsilon_{ij}^{b}\,{}^ih + {}^i\varepsilon_{ij}^{u}\left({}^iL - {}^ih\right)\right] + \frac{1}{{}^jL}\left[\varepsilon_{ij}^{b}\,{}^jh + {}^j\varepsilon_{ij}^{u}\left({}^jL - {}^jh\right)\right]\right\} \tag{31}
$$

The next set of equations is obtained by enforcing equilibrium in each direction between the corresponding stress components in the elastic zone and in the localization band. For each

direction m, the following condition must be satisfied:

$$\sigma_{ij}^{b}\,{}^{m}e_j = {}^{m}\sigma_{ij}^{u}\,{}^{m}e_j \quad \text{for } m = 1\ldots3 \tag{32}$$

where ${}^{m}e_j$ denotes co-ordinates of a unit direction vector for principal strain direction m. Since the principal frame of the total macroscopic strain tensor is used, the unit vectors have the following co-ordinates:

$${}^{1}e_j = (1,0,0), \quad {}^{2}e_j = (0,1,0), \quad {}^{3}e_j = (0,0,1) \tag{33}$$

The remaining equations are obtained by enforcing equilibrium between tractions on the other surfaces of the band and the elastic zone imagined as a spring:

$$\sigma_{ij}^{b}\,{}^{m}e_j = {}^{n}\sigma_{ij}^{u}\,{}^{m}e_j \quad \text{where } m = 1\ldots3,\ n = 1,\ldots3,\ m \neq n \tag{34}$$

It should be noted that this is different from the one-dimensional localization element where the kinematic constraint (11) was used for these surfaces. Equation (34) is equivalent to a static constraint on the remaining stress and strain components of the elastic springs. Formulas (32) and (34) together with the assumption of stress tensor symmetry represent the remaining 18 equations that are needed for the solution of the three-dimensional equivalent localization element. These 18 equations can be written as

$$\sigma_{ij}^{b} = {}^{m}\sigma_{ij}^{u} \quad \text{for } m = 1,\ldots3 \tag{35}$$

This means that the macroscopic stress must be equal to σ_{ij}^{b}, i.e. the stress in the localization element, and that the stresses in all the three elastic zones must be equal to each other and to the microplane stress σ_{ij}^{b}. This implies also the equivalence of all the three elastic strain tensors.

Based on the foregoing derivations, and in analogy to the derivations in Section 4, it is possible to formulate an algorithm for the calculation of unknown quantities in the three-dimensional equivalent localization element.

Input:

$$\varepsilon_{ij},\ \Delta\varepsilon_{ij},\ \varepsilon_{ij}^{b},\ \varepsilon_{ij}^{u} \tag{36}$$

Initialization:

$$\Delta\varepsilon_{ij}^{b} = \Delta\varepsilon_{ij}^{u} = \Delta\varepsilon_{ij} \tag{37}$$

Step 1:

$$\mathrm{d}\varepsilon_{ij}^{u(i)} = \frac{{}^{i}L\ {}^{j}h + {}^{j}L\ {}^{i}h}{2\,{}^{i}L\ {}^{j}L}\, C_{ijkl} r_{kl}^{(i-1)} \tag{38}$$

Step 2:

$$\Delta\varepsilon_{ij}^{u(i)} = \Delta\varepsilon_{ij}^{u(i-1)} + \mathrm{d}\varepsilon_{ij}^{u(i)} \tag{39}$$

Step 3:

$$\Delta\varepsilon_{ij}^{b(i)} = \frac{2\,{}^{i}L\ {}^{j}L}{{}^{i}L\ {}^{j}h + {}^{j}L\ {}^{i}h}\,\Delta\varepsilon_{ij} - \frac{2\,{}^{i}L\ {}^{j}L - {}^{i}L\ {}^{j}h - {}^{j}L\ {}^{i}h}{{}^{i}L\ {}^{j}h + {}^{j}L\ {}^{i}h}\,\Delta\varepsilon_{ij}^{u} \tag{40}$$

Step 4:

$$r_{ij}^{(i)} = \sigma_{ij}^{b(i)} - \sigma_{ij}^{u(i)} \tag{41}$$

where C_{ijlk} is the compliance tensor. Equation (38) is obtained in analogy to Equation (25), but this time Equation (31) is used for the calculation of the partial derivative $\partial\varepsilon_{ij}^{b}/\partial\varepsilon_{ij}^{u}$. It can be easily verified that, by setting ${}^1L = {}^2L = {}^3L = L$ and ${}^1h = {}^2h = {}^3h = h$, Equation (25) is recovered. Similar convergence criteria as in Section 4 can be used;

$$\frac{\|\mathrm{d}\varepsilon_{ij}^{u(i)}\|}{\|\Delta\varepsilon_{ij}\|} < e, \quad \frac{\|r_{ij}^{(i)}\|}{\|\Delta\sigma_{ij}^{b}\|} < e, \quad \frac{|r_{ij}^{(i)T}\,\mathrm{d}\varepsilon_{ij}^{u(i)}|}{\|\Delta\sigma_{ij}^{b}\Delta\varepsilon_{ij}\|} < e \tag{42}$$

The macroscopic stress is then equal to the stress in the localization band σ_{ij}^{b}. Contrary to the one-dimensional localization element there are no restrictions. All the types of localization modes and all directions of failure propagation can be considered.

6. EXAMPLES OF APPLICATION

Now, it is possible to demonstrate applications of the proposed equivalent localization element to four example problems. The goal is to investigate the objectivity of results with respect to the element size that is achieved when the equivalent localization elements are used. The finite element method is employed, and always several finite element sizes are used to demonstrate the mesh size objectivity. The same example problems and same meshes with the microplane model are calculated for comparison, also without the equivalent localization elements, and the comparison is used to make the benefits of the proposed approach conspicuous. All the examples presented in this paper are calculated by the code ATENA [14]. This is an implicit finite element which incorporates the object-oriented approach and template meta-programming. The examples presented involve plane stress calculations, while the developed model is fully 3D. This is facilitated by an internal feature of the code ATENA enabling the application of 3D models in 2D configurations. The material driver internally calculates the out-of plane strain components based on the assumption that, in the case of plane stress idealization, the corresponding transverse normal stress components must be zero.

6.1. Single large element in tension

The first example is a specimen under uniaxial tension. The geometry of the problem corresponds to tension specimens tested by Hordijk [15]. Three specimens with the same cross-sectional area but with different lengths are analysed. The dimensions and geometry are shown in Figure 4.

When large finite elements are used in a finite element calculation that is dominated by tensile material failure, each element should correctly reproduce the macroscopic behaviour of the tensile test. For this reason every specimen is modelled by only one finite element, each of a different length. Each test should reproduce the macroscopic behaviour of the corresponding uniaxial tensile test. All the specimens are loaded by prescribed displacement, and the reaction forces are monitored during the analysis.

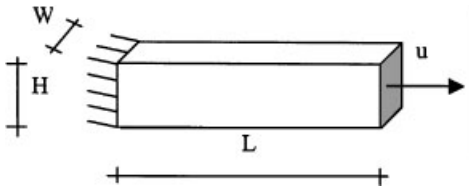

Specimen	Length [mm]	Width [mm]	Height [mm]
A	250	50	50
B	125	50	50
C	50	50	50

Figure 4. Tensile specimen geometry, dimensions and loading.

The results of numerical analysis are compared with the experiment of Hordijk [15]. The following material properties of concrete were measured: the modulus of elasticity $E = 18,000\,\text{MPa}$, cubic compressive strength $f_{\text{cu}} = -50.4\,\text{MPa}$, tensile strength $f_{\text{t}} = 3.3\,\text{MPa}$, and maximum aggregate size $d_{\max} = 2\,\text{mm}$. The default material parameters of the microplane model are used in the analysis ($k_2 = 500$, $k_3 = 15$, $k_4 = 150$), with the exception of the microplane parameter k_1 that was determined as $k_1 = 3.43 \times 10^{-4}$ by fitting the measured tensile strength. This value of k_1 is to be compared to the value that would be determined from the prediction formulae proposed by Caner and Bažant [13]:

$$k_1^* = k_1 \frac{\varepsilon_p^*}{\varepsilon_p} = 2.45 \times 10^{-4} \frac{0.0048}{0.0036} = 3.27 \times 10^{-4} \tag{43}$$

The difference between this value and the value used in the analysis is not substantial, and can be attributed to the fact that the prediction formula assumes a ratio of compressive and tensile strength slightly different from these experiments. Indeed the formula corresponds to $f_t'/f_c' = 0.068$, while the concrete used is characterized by the ratio 0.077, which means that a higher value of k_1 can be expected. In Equation (43), ε_p is the strain at compressive strength in a uniaxial test. The superscript star indicates the values for the specified concrete type, and the quantities without such a superscript are the reference values for concrete with the compressive strength of 46 MPa. Two finite element analyses are performed for each geometry: one with the equivalent crack band model and one without it. The crack band size h is set to $1.5\,d$, where d be the aggregate size, i.e. $h = 3\,\text{mm}$.

Figure 5 shows the calculated stress–strain relations for all the specimens. The solid curve represents the calculations, in which the equivalent localization element is used. The dashed curves are calculated by the standard microplane model. The initial stiffness depends on the specimen length, L.

The figure shows that the specimens failed at the same tensile stress level. The post-peak behaviour from the analyses with the equivalent localization element depends on the specimen length. Not surprisingly, for longer elements, the response is seen to be more brittle than for shorter ones. This is in a good agreement with the experimental observations, and contrasts with the results calculated without using the localization element. In this case the post-peak response does not depend on the element size at all and is very ductile. This result agrees with what is expected because the microplane model is calibrated for element sizes close to the material characteristic length and, as is true for any strain-softening material model, cannot be used for much larger finite elements.

The next Figure 6 depicts the same results, but the deformation corresponds to the crack opening displacements as they were measured in the experiment. The computed data are

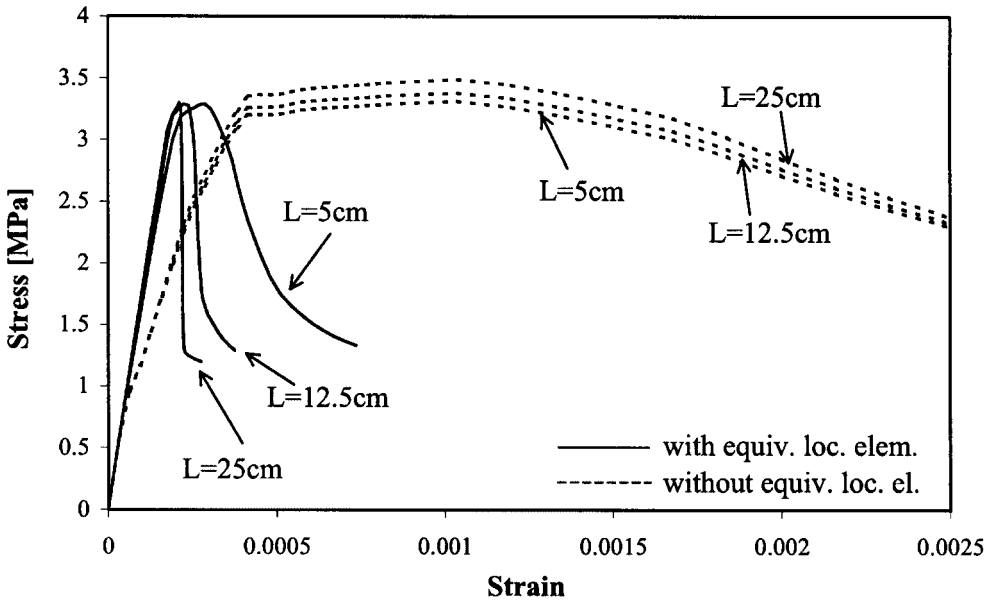

Figure 5. Stress–strain diagrams from the tension test.

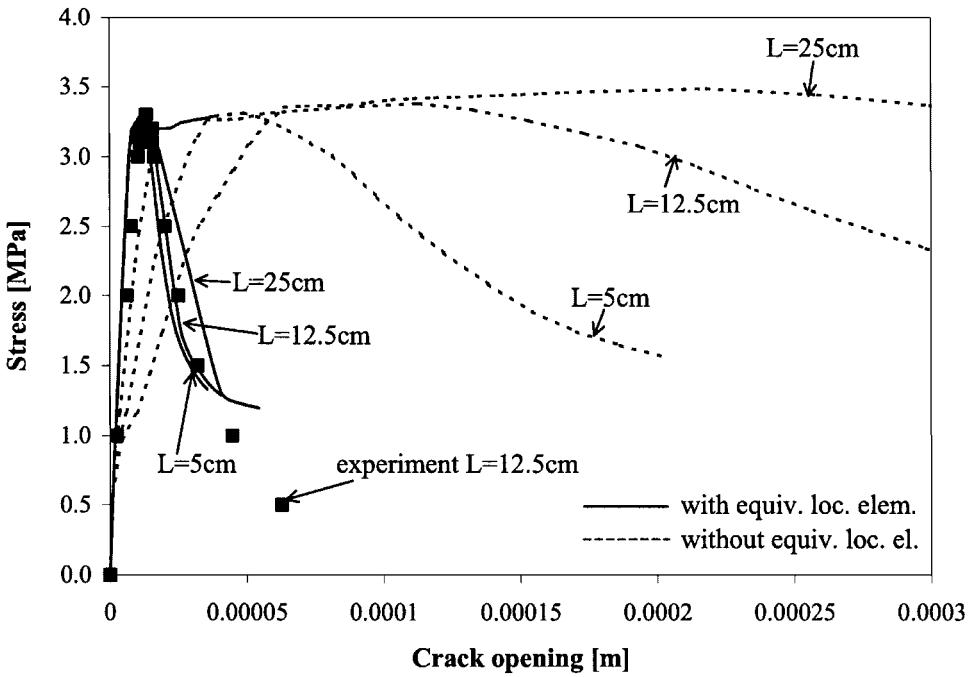

Figure 6. Stress—crack opening displacement diagrams from the tension test.

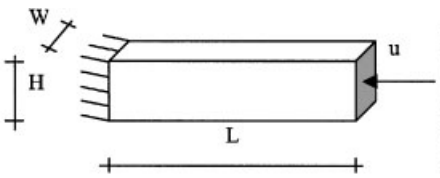

Specimen	Length [mm]	Width [mm]	Height [mm]
A	200	100	100
B	100	100	100
C	50	100	100

Figure 7. Compressive specimen geometry, dimensions and loading.

compared with the measurements of Hordijk [15]. The measured displacement does not correspond exactly to the pure crack opening displacement, which is doubtless due to the fact that it was measured over the base length of 35 mm spanning the notch, and thus contains some elastic displacements. This elastic component was also considered in the comparison, and is included in the numerical results as well. This figure clearly shows the benefits of the proposed method. It can correctly reproduce the crack opening law, independently of the finite element size. This is sharply contrasted by the results from the plain microplane model, in which a strong dependence on the finite element size can be observed.

6.2. Single large element in compression

The second example problem is similar to the first, but a compressive behaviour is considered. Prisms with a square cross-section and with different lengths are analysed using a single finite element. Each analysis should be able to reproduce the behaviour of a similar experiment. In this case, the experimental data by van Mier [16] are used for comparison.

Figure 7 shows the important dimensions and geometry of the tested specimens. Van Mier [16] reports the following basic material properties: the elastic modulus $E = 28,000$ MPa, cubic strength $f_{cu} = 42.6$ MPa, and maximum aggregate size $d_{max} = 16$ mm. The default material parameters of microplane model M4 are again used in the analysis ($k_2 = 500$, $k_3 = 15$, $k_4 = 150$), with the exception of the microplane parameter k_1, which was adjusted by fitting the measured compressive strength; the resulting optimum value used in the analysis was $k_1 = 1.72 \times 10^{-4}$. This is not too different from the value that ensues from the empirical formula given by Caner and Bažant [13]:

$$k_1^* = k_1 \frac{\varepsilon_p^*}{\varepsilon_p} = 2.45 \times 10^{-4} \frac{0.0024}{0.0036} = 1.63 \times 10^{-4} \tag{44}$$

The specimens considered are loaded by prescribed displacement (Figure 7), and the reaction forces are monitored and used for the stress calculation. Again the numerical model is formed by a single finite element. Two analyses are performed for each length: one with localization element and one without it. In the first case, two crack band sizes are used. For the directions of the negative principal strains, $h_- = 3\,d_{max} = 48$ mm, while for the directions of the positive principal strains, $h_+ = 1.5\,d_{max} = 24$ mm. The stress–strain relations are shown in Figures 8 and 9. The curves show a strong size effect of the post-peak response. This effect is very well reproduced by the analyses with localization element, but is not reproduced at all by the plain microplane model. As expected, the results without localization element do not exhibit any size effect.

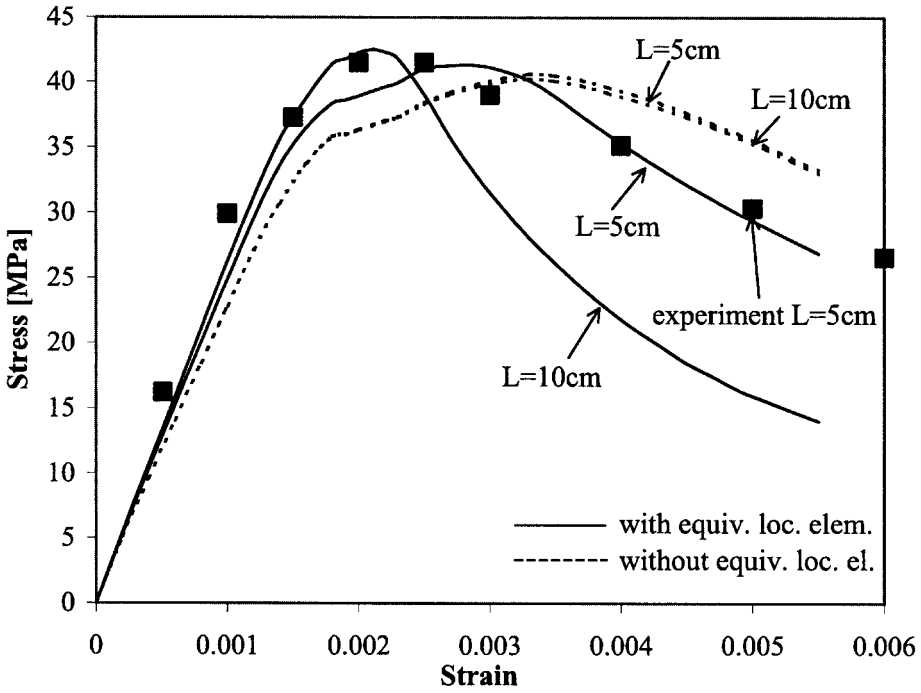

Figure 8. Stress–strain diagrams (experiment, $L = 5$ cm).

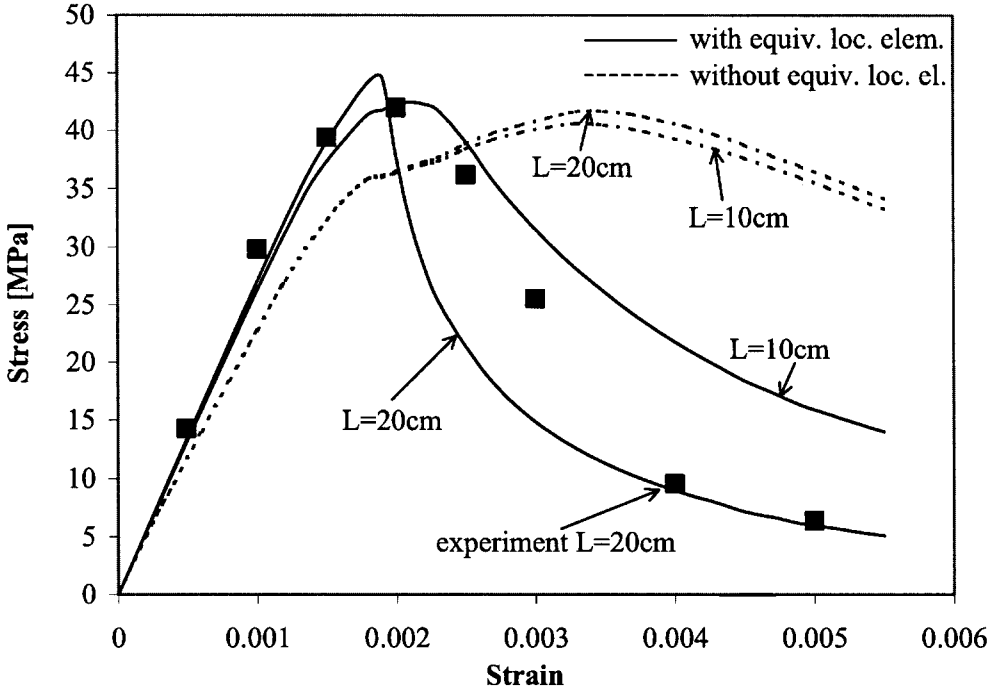

Figure 9. Stress–strain diagrams (experiment, $L = 20$ cm).

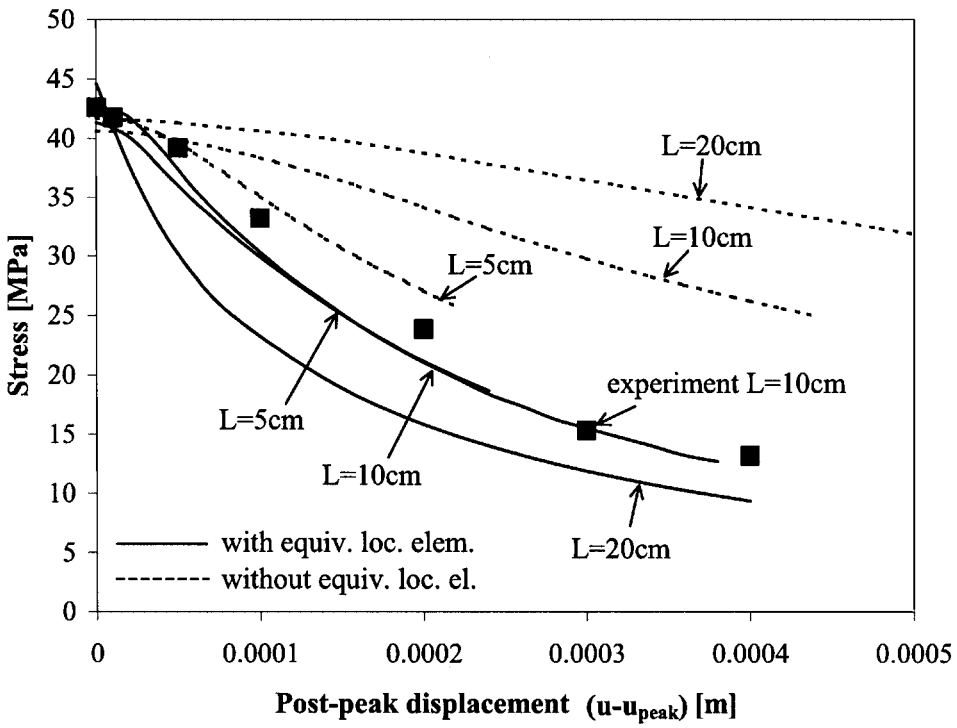

Figure 10. Post-peak stress–displacement diagrams $(u - u_{\text{peak}})$.

Figure 10 demonstrates another effect that was documented by van Mier [16]. He observed that, if the displacement at peak is subtracted from the total displacement, the post-peak curves obtained are approximately independent of the specimen length. This experimental observation is well reproduced by the localization element.

6.3. Three-point bending beam with different mesh sizes and comparison with experiments

The next example is a slightly more complex problem of an unreinforced concrete beam that is subjected to three-point bending (Figure 11). The analysed beam corresponds to the beams tested by Uchida [17]. The beam had dimensions $100 \times 100 \times 840$ mm.

The measured material properties were as follows: the elastic modulus $E = 21,300$ MPa, cubic compressive strength $f_{\text{cu}} = 39.9$ MPa, the maximum aggregate size $d_{\max} = 15$ mm. The same default material parameters as in the preceding sections were used in the microplane model ($k_2 = 500$, $k_3 = 15$, $k_4 = 150$), with the exception of parameter k_1 which was determined as $k_1 = 1.10 \times 10^{-4}$, by fitting the peak load. The formula of Caner and Bažant [13] gives

$$k_1^* = k_1 \frac{\varepsilon_p^*}{\varepsilon_p} = 2.45 \times 10^{-4} \frac{0.0032}{0.0036} = 2.18 \times 10^{-4} \tag{45}$$

The large difference between the k_1 value used here and the value from the formula can again be explained by the fact that Equation (45) assumes the ratio of the tensile to compressive

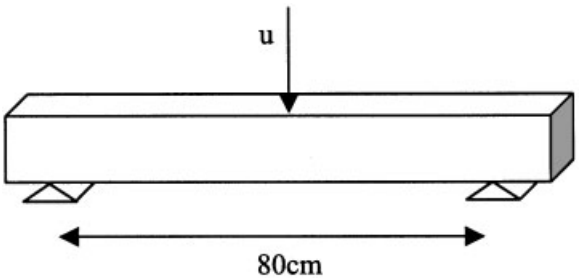

Figure 11. Geometry and loading of three-point-bend beam.

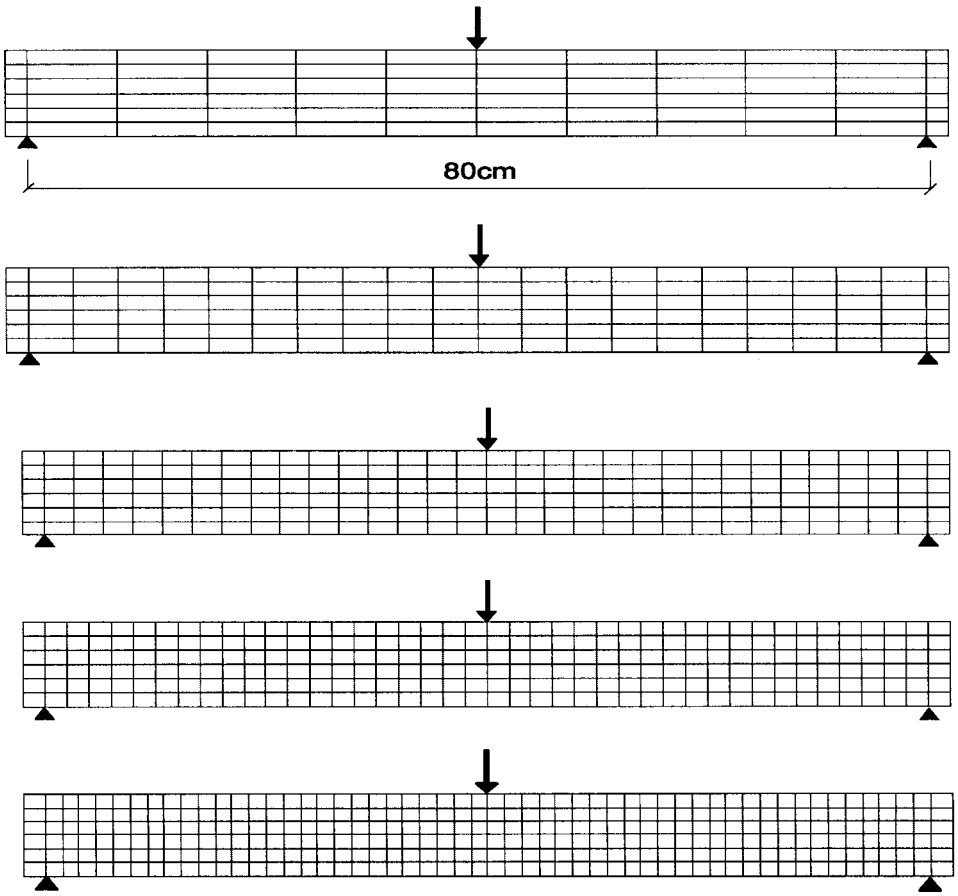

Figure 12. Finite element meshes for the three-point-bend beam.

strength to be 0.068, which may differ from reality. In addition, the value of ε_p^* is not known for this problem, and it was assumed as $\varepsilon_p^* = 2f_c'/E$.

Five finite element meshes are used in this example: a fine mesh with an element size of 16.6×20 mm ($S = 2$ cm), a medium mesh with an element size of 16.6×26.7 mm

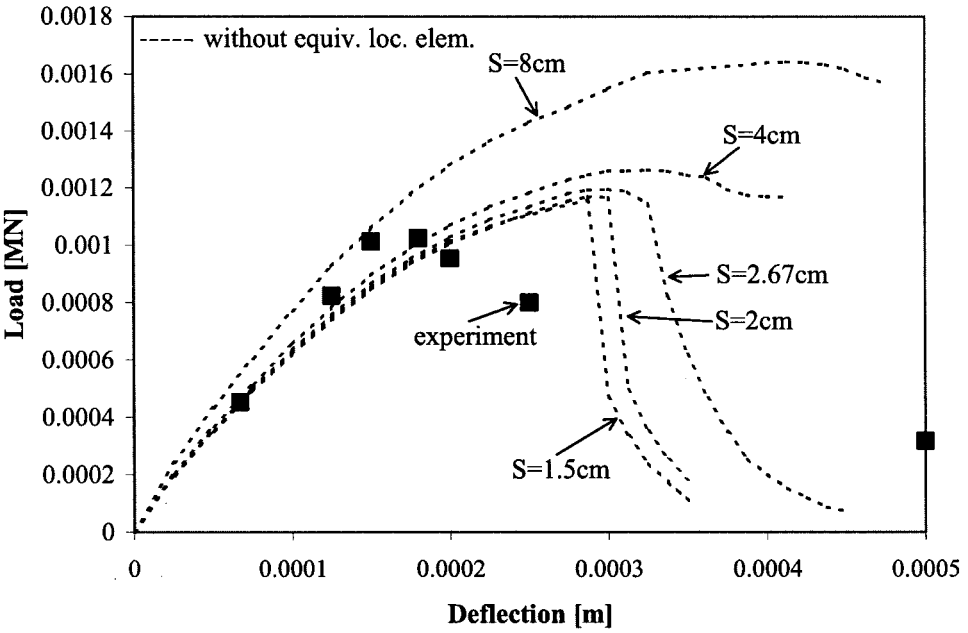

Figure 13. Load–deflection diagram from three-point-bend beam computations without localization elements.

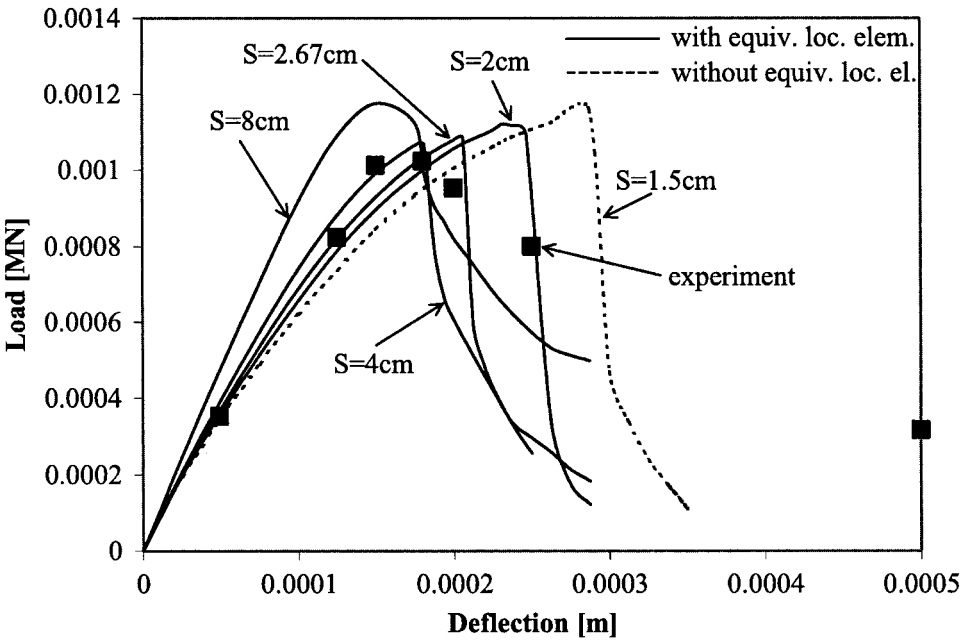

Figure 14. Load–deflection diagram from three-point-bend computations with localization elements.

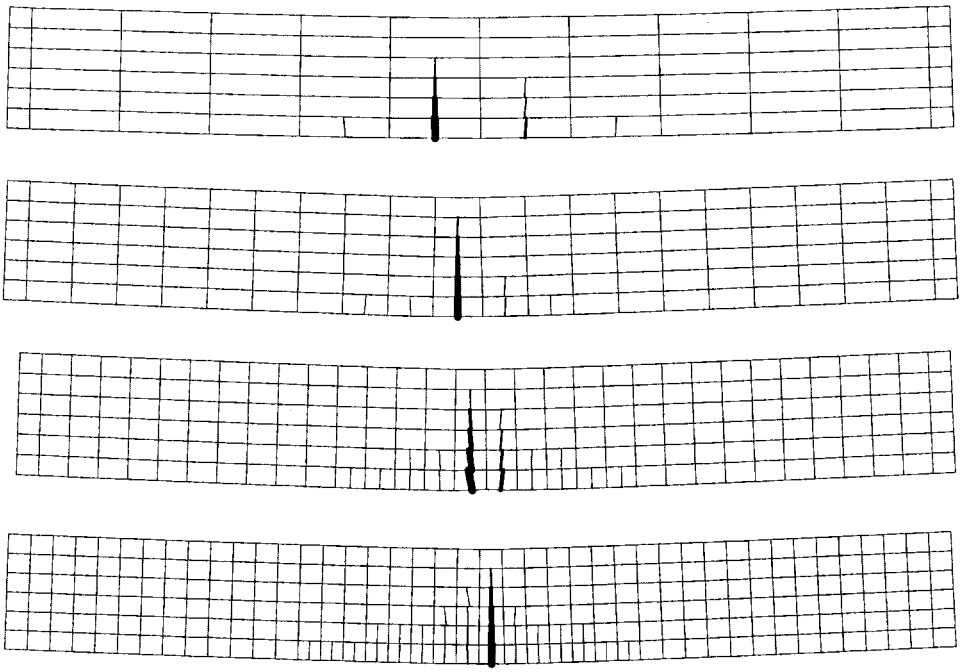

Figure 15. Deformed shapes of the three-point-bend beam with cracks, computed with localization elements.

($S = 2.67$ cm), a medium mesh with element size 16.6×40 mm ($S = 4$ cm), a coarse mesh with element size 16.6×80 mm ($S = 8$ cm), and also a mesh with element size of 16.6×15 mm ($S = 1.5$ cm) as the finest mesh (Figure 12). Two analyses are performed for the first four meshes: one with the localization elements and one without them. The crack band size h is set to 15 mm in the localization element analyses. The fifth mesh is used as a comparison, and the proper element size for M4 model is used (no localization element is involved). The models were loaded by prescribed displacement at mid-span, and the Newton–Raphson method with line-search iterations was used in all computations.

The results (Figures 13 and 14) clearly show that the localization element gives a much more consistent and less mesh size dependent results. The post-peak response is more brittle than it is in the experiment, which can be attributed to the fact that the crack band parameter is set to $h = d_{\max}$ rather then to $h = 1.5\, d_{\max}$.

In addition, note that all the results presented in this paper are obtained with the default parameters of microplane model M4, with minimal fitting of any data. The post-peak response could be also adjusted by the microplane parameter c_3 (see Caner and Bažant [13]). For practical engineering calculation, however, the peak load and the pre-peak response are the most important aspects of structural behaviour.

Figure 15 shows the calculated deformed shapes and crack patterns for all the four meshes with the localization element.

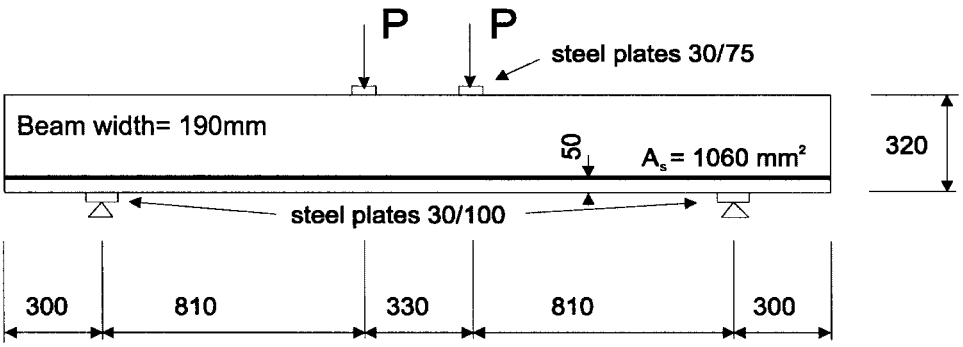

Figure 16. Geometry of beam tested for shear by Leonhard and Walter.

6.4. Leonhardt and Walther's reinforced concrete beam failing in shear

This example shows a simply supported reinforced concrete beam without shear reinforcement. Effects of the finite element mesh and of the crack band size on the shear failure of the beam are investigated. This example involves a complex failure mode with tensile cracking, crack shearing and compressive strut crushing. The geometry, loading, material properties and results are obtained from the work of Leonhardt and Walther [18]. The dimensions are given in Figure 16. The measured material properties of concrete were the modulus of elasticity $E = 35,950\,\text{MPa}$ and the cylindrical uniaxial compressive strength $f_c' = -28.5\,\text{MPa}$. The steel properties were the modulus of elasticity $E = 210,000\,\text{MPa}$ and the yield stress $f_y = 400\,\text{MPa}$. The default material parameters of microplane model M4 were again used, as before ($k_2 = 500$, $k_3 = 15$, $k_4 = 150$), with the exception of parameter k_1 which was determined by fitting the peak load. The final value of this parameter is set to $k_1 = 0.867 \times 10^{-4}$ while Caner and Bažant's formula [13] gives

$$k_1^* = k_1 \frac{\varepsilon_p^*}{\varepsilon_p} = 2.45 \times 10^{-4} \frac{0.0018}{0.0036} = 1.23 \times 10^{-4} \tag{46}$$

The finite element models, which take advantage of symmetry of the beam, are shown in Figure 17. The fine mesh has 12 elements along the height, the medium mesh six elements, the coarse mesh four elements and again the finest mesh (extra fine mesh), where the proper element size is chosen for model M4, has 18 elements. In the computational model, the loading consists of prescribed displacement, and the reaction forces are calculated. Two computations are performed: with and without the localization elements. The crack band size is set to $h = 25$ mm. The calculated results without localization elements, with localization elements, and with a proper element size (fixed, without localization elements) are shown in Figures 18 and 19, respectively. The subsequent Figure 20 depicts the deformed meshes for the analyses with localization elements.

The load–deflection diagrams again demonstrate the practical applicability of the proposed equivalent localization element. The diagrams calculated with the localization elements are much less sensitive to element size and they predict the peak load very well. The post-peak response was not measured in the experiment but may be expected to be more brittle than the computed one. Also, the crack pattern that is depicted in Figure 20 differs from the experimental

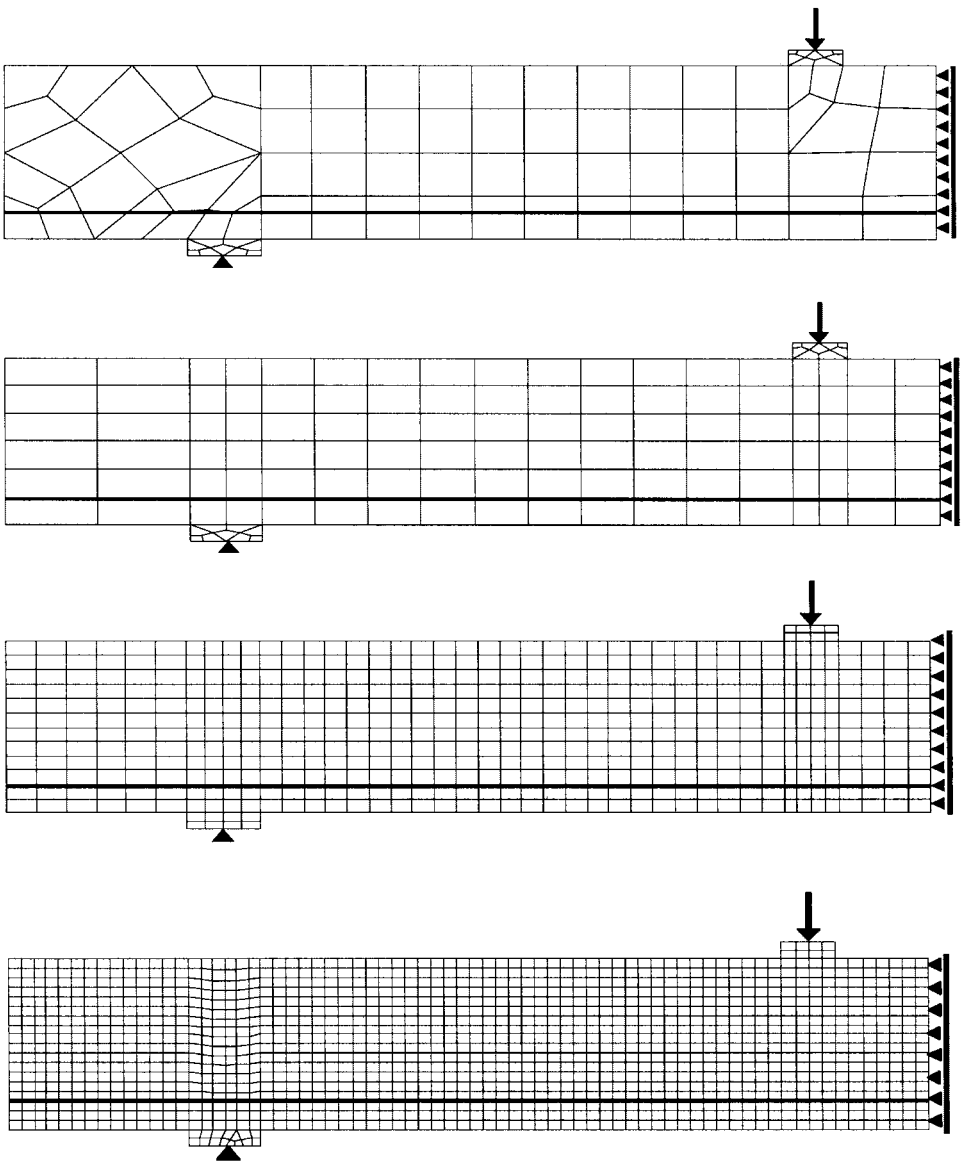

Figure 17. Finite element meshes for the shear beam test.

observation. In the experiment, a diagonal crack with greater inclination is observed, and the failure of reinforcement bond is not as dominant as in the computations.

Note that this analysis is again performed with the default material parameters of microplane model M4, with minimal fitting, consisting merely in vertical scaling of constitutive model curves by parameter k_1 so as to match the measured material strength. In spite of that, the accuracy of results is satisfactory for most practical purposes.

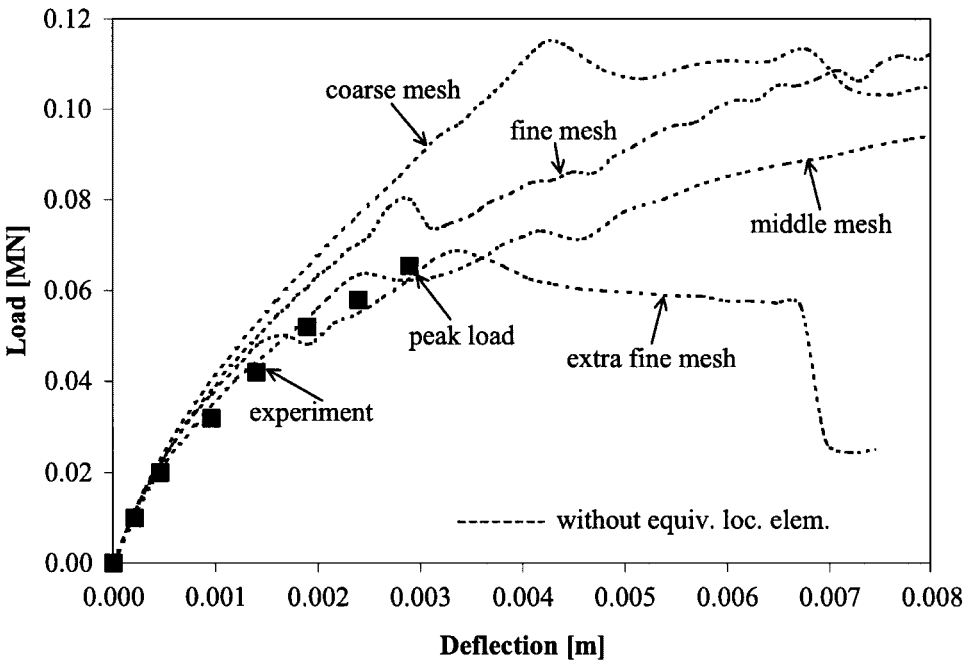

Figure 18. Load–deflection diagram for the shear beam test computed without localization elements.

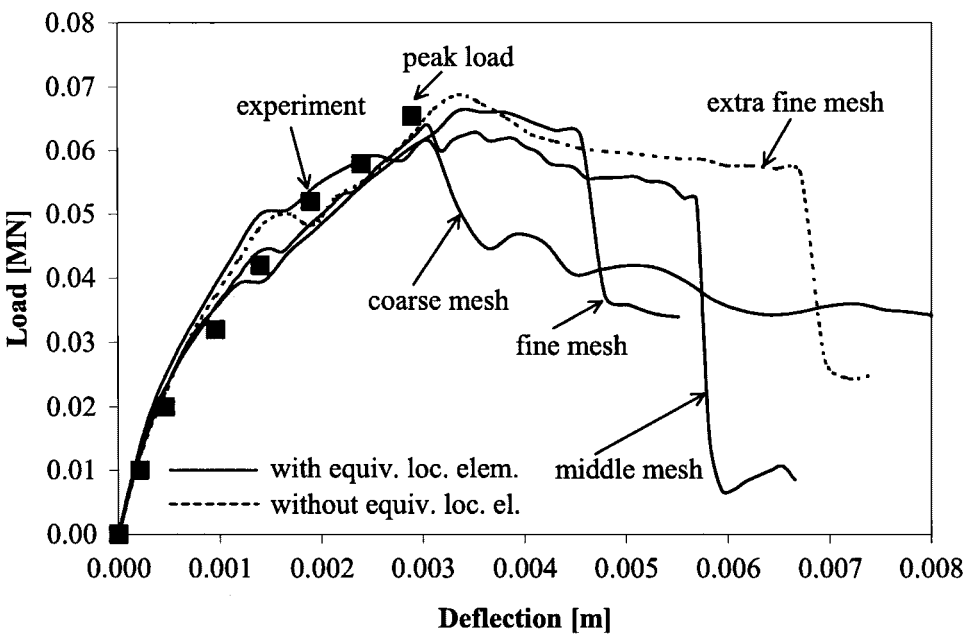

Figure 19. Load–deflection diagram for the shear beam test computed with localization elements (crack band width $h = 25$ mm).

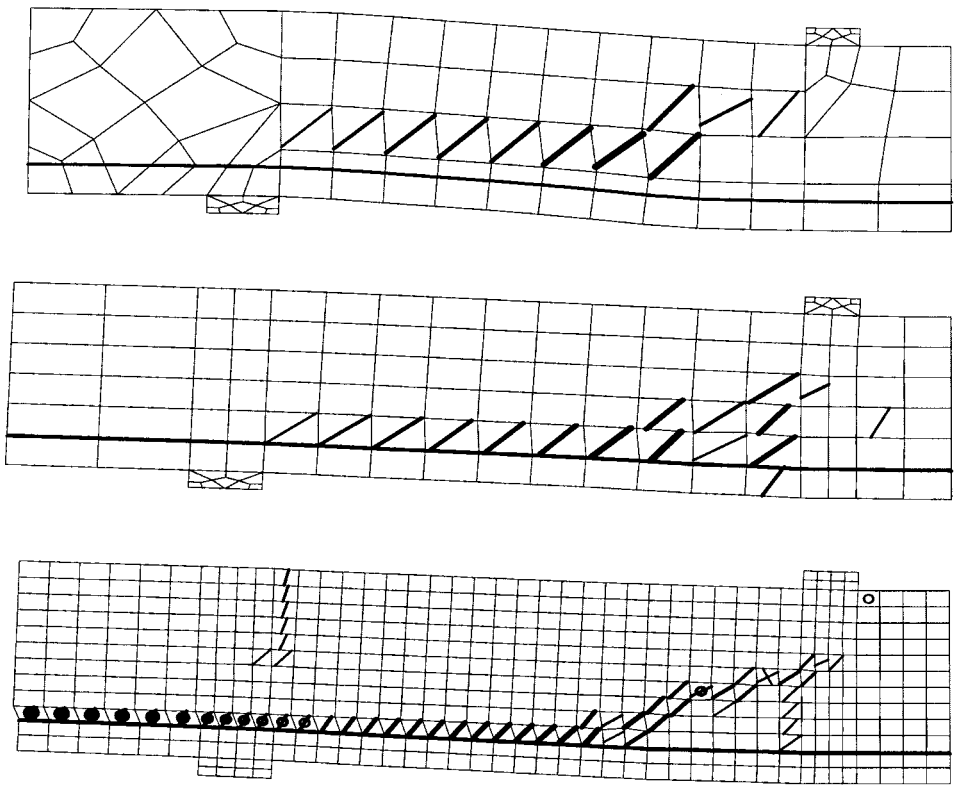

Figure 20. Deformed shapes and crack patterns from shear beam test computations.

Comparisons of numerical efficiency of these two approaches for this non-trivial example are of interest. A computer with Celeron 600 MHz, 196 MB RAM was used for all computations. The results of this study (obtained on a PC with Celeron 600 MHz and RAM 196 MB) are summarized in Figures 21 and 22. The former shows the total computing time, including memory allocation for the variables, assembly of stiffness matrices, etc. The latter shows the time increase due to applying the localization elements. The computing time is increased approximately by the factor of 2.5. It should be realized that such an increase is balanced with the possibility of using coarser meshes while preserving similar accuracy. For example, the total time for the model with extra-fine mesh, for which the localization elements are not needed, is 50, 000 s. If the medium mesh is used, the time decreases to 18, 000 s while preserving the same accuracy.

7. CLOSING COMMENTS AND CONCLUSIONS

This paper presents in detail a novel method for implementing complex material models such as the microplane model in finite element programs. This method allows objective use of

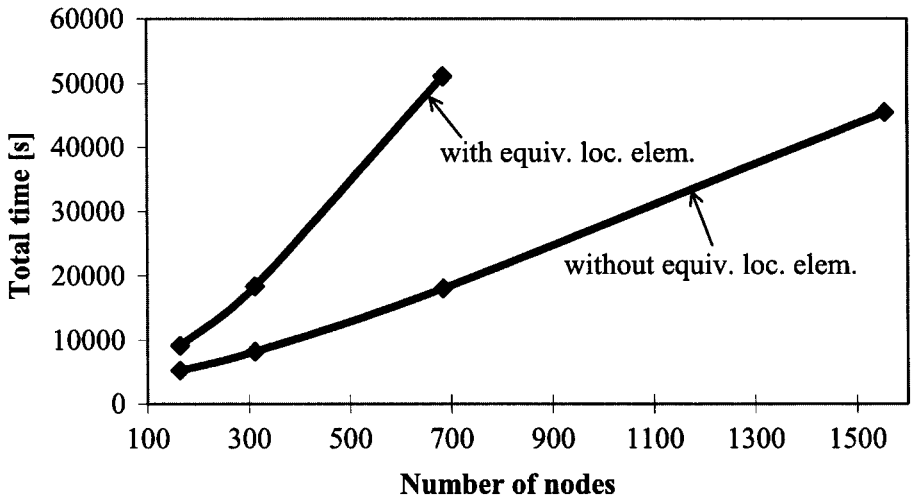

Figure 21. Total computer time (in s) of shear beam analysis for different meshes.

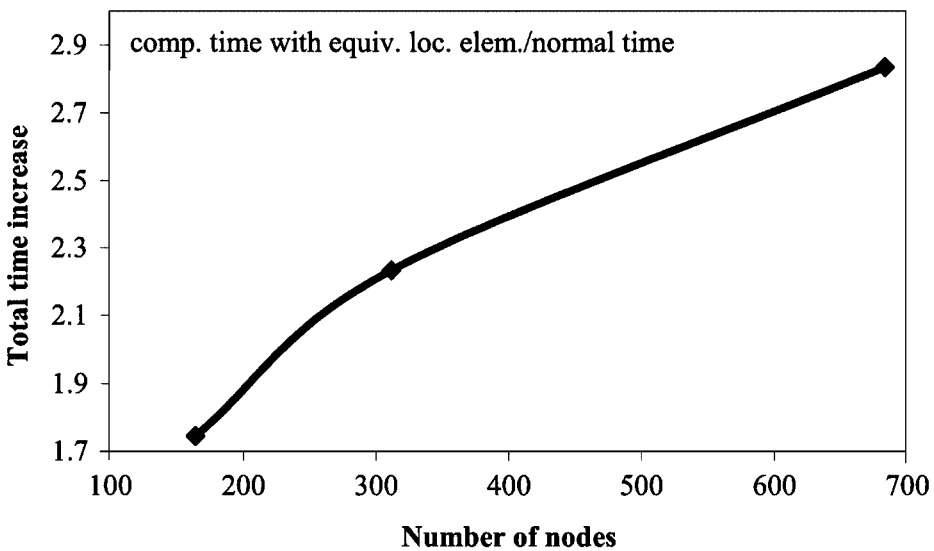

Figure 22. Total increase in time due to including localization elements in shear beam test analysis.

complex stress–strain relations with softening in finite element analyses with large element sizes. The only additional parameter is the width h of the localization band, which physically corresponds to the characteristic length of the material for which the material formulation has been calibrated. For concrete, the band width should be roughly equal to about $1.5d_{\max}$, where $d_{\max}$ is the maximal size of concrete aggregates. The underlying assumption is that only one localization zone develops in a single finite element. This zone is assumed to be coupled as a

layer with an elastically unloading zone, called the 'spring'. In the current implementation, one spring is aligned with each principal strain direction. Different widths h can be used for each direction. Here, two different values of h are used: $h = 1.5\, d_{\max}$ for directions with positive principal strain, and $h = 3 d_{\max}$ for directions with negative principal strain. The different values of h are introduced to differentiate between tensile fracturing and compressive crushing.

A disadvantage of the proposed method is the necessity to evaluate the microplane model several times, which considerably increases the computational time. Typically, about 8 iterations are needed in the proposed iterative algorithms (26) and (38)–(41). The developed method is applicable only for element sizes larger than, or equal to, the characteristic length. When the element size is smaller, the equivalent crack band method is deactivated and the normal stress-strain formulation is used. However, for such element sizes a non-local model should properly be used because otherwise the present approach would underestimate the energy dissipation in post-peak softening and thus yield over-conservative results regarding failure.

The proposed approach is demonstrated using microplane model M4 by Bažant *et al*. [12], but is suitable for other material models as well. It suppresses the mesh size sensitivity of strain-softening material models.

The sensitivity of finite element crack band model to mesh orientation cannot be addressed by this approach. This sensitivity can be alleviated by a penalty coefficient for crack band propagation directions not aligned with the mesh line [19, 20], and can be completely overcome by using some non-local techniques and small finite element sizes not exceeding about $0.3h$. The proposed method can be used to supplement non-local concepts so as to eliminate the need for using very small finite elements. The averaging volume in the non-local concept does not have to be fixed, but it can depend on finite element size, such that the number of element, within the averaging volume would suffice to eliminate the mesh orientation bias. The size averaging volume in the non-local approach, needed to eliminate mesh bias, will correspond to the size of the equivalent crack band element L, and h would physically represent the width of the localization zone.

ACKNOWLEDGEMENTS

This work was initiated during a Visiting Scholar appointment of J. Červenka at Northwestern University in 1999 supported by the U.S. National Science Foundation (NSF) under Grant CMS-9732791, and completed during a Visiting Fellow appointment of M. Wierer at Northwestern University in 2003 supported by NSF under Grant CMS-030145. These grants also supported the work of Z. P. Bažant (grant director). Further work during 2000–2001 was carried out at Červenka Co., Prague, under contract 103/99/0755 with the Czech Grant Agency.

REFERENCES

1. Bažant ZP. Crack band model for fracture of geomaterials. In *Proceedings of the 4th International Conference on Numerical Mathematics in Geomechanics*, vol. 3, Eisenstein Z (ed.), held at University of Alberta, Edmonton, 1982; 1137–1152.
2. Bažant ZP. Instability, ductility, and size effect in strain-softening concrete. *Journal of Engineering Mechanics Division* (ASCE) 1976; **102**(EM2):331–344.
3. Bažant ZP, Oh BH. Crack band theory for fracture of concrete. *Materials and Structures*, vol. 16. RILEM: Paris, France, 1983; 155–177.
4. Bažant ZP, Planas J. *Fracture and Size Effect in Concrete and Other Quasibrittle Materials*. CRC Press: Boca Raton and London, 1998.

5. Pietruszczak St., Mróz Z. Finite element analysis of deformation of strain-softening materials. *International Journal for Numerical Methods in Engineering* 1981; **17**:327–334.
6. Bažant ZP, Belytschko TB, Chang TP. Continuum model for strain softening. *Journal of Engineering Mechanics* (ASCE) 1984; **110**(12):1666–1692.
7. Pijaudier-Cabot G, Bažant ZP. Nonlocal damage theory. *Journal of Engineering Mechanics* (ASCE) 1987; **113**(10):1512–1533.
8. Bažant ZP, Jirásek M. Nonlocal integral formulations of plasticity and damage: survey of progress. *Journal of Engineering Mechanics* (ASCE) 2002; **128**(11):1119–1149.
9. Bažant ZP. Microplane model for strain controlled inelastic behavior. In *Mechanics of Engineering Materials*, Chapter 3 (Proceedings of the Conference held at University of Arizona, Tucson, January 1984), Desai CS, Gallagher RH (eds). Wiley: London, 1984; 45–59.
10. Taylor GI. Plastic strain in metal. *Journal of Institution Metals* 1938; **62**:307–324.
11. Bažant ZP, Červenka J, Wierer M. Equivalent localization element for crack band model as alternative to elements with embedded discontinuities. *Fracture Mechanics of Concrete Structures* (Proceedings of the International Conference FraMCoS, Paris), de Borst R *et al*. (eds). Swets & Zeitlinger, A.A. Balkema Publishers: Lisse, Netherlands, 2001; 765–772.
12. Bažant ZP, Caner FC, Carol I, Adley MD, Akers SA. Microplane model M4 for concrete: I. formulation with work-conjugate deviatoric stress. *Journal of Engineering Mechanics* (ASCE) 2000; **126**(9):944–961.
13. Caner FC, Bažant ZP. Microplane model M4 for concrete: II. algorithm and calibration. *Journal of Engineering Mechanics* (ASCE) 2000; **129**(9):954–961.
14. ATENA, *Program Documentation*. Červenka Consulting, www.cervenka.cz, 2000.
15. Hordijk DA. Local approach to fatigue of concrete. *Thesis*, Technische Universiteit Delft, W.D. Meinema b.v. Delft, p. 47 (1991).
16. van Mier JGM. *Fracture of Concrete under Complex Stress*, vol. 3. HERON: Delft, Netherlands, 1986; 23.
17. Uchida Y, Kurihara N, Rokugo K, Koyanagi W. Determination of tension softening diagrams of various kinds of concrete by means of numerical analysis. *Fracture Mechanics of Concrete Structures*. Aedificatio Publishers: Freiburg, 1995; 25.
18. Leonhardt F, Walther R. *Schubversuche an einfeldrigen Stahlbetonbalken mit und ohne Schubbewehrung*. Deutscher Ausschuss für Stahlbeton, vol. 56 (no. 12) 1961, vol. 57 (no. 2,3,6,7,8) 1962, and vol.58 (no. 8,9) 1963. Ernst & Sohn: Berlin, 1962.
19. Bažant ZP. Mechanics of fracture and progressive cracking in concrete structures. *Fracture Mechanics of Concrete*: *Structural Application and Numerical Calculation*, Chapter 1, Sih GC, Tommaso AD (eds). Martinus Nijhoff: Dordrecht and Boston, 1985; 1–94.
20. Červenka V. Applied brittle analysis of concrete structures. *3rd International Conference on Fracture Mechanics of Concrete Structures* (FraMCoS-3, held in Gifu, Japan, Post-conference Supplement to Proceedings), 1998; 1–15.

